PHILOSOPHICAL TRANSACTIONS A

royalsocietypublishing.org/journal/rsta

Research

Article submitted to journal

Subject Areas:
two-phase flow, droplets trajectories, numerical schemes, linear solvers, turbulence models, ice shape, ice accretion, rime

Keywords:
aircraft icing, CFD, ice shapes, icing simulation, impingement, TVD

Author for correspondence:
Guilherme Araujo Lima da Silva
e-mail: gasilva@aerothermal.co

Introducing the iceAccretionFoam Solver: Impingement and Rime Ice

Jayme R. Teixeira da Silva[1], Pedro C. de Souza Villela[1], Caio F. Rafael[2], Guilherme A. Lima Silva[2] and Hrvoje Jasak[3,4]

[1]Av. Pompéia, 634 cj 107, Sao Paulo, SP, Brazil
[2]201 Biscayne Blvd., Suite 1200, Miami, FL, USA
[3]Cambridge University, Cambridge, UK
[4]459 Southbank House, London, UK

This paper explores the capabilities of iceAccretionFoam, an innovative solver developed on top of the Foam-extend 5.0 code, for computing icing in two-dimensional domains, performed on a NACA0012 airfoil. The study presents droplet transport carried out by an incompressible unsteady Reynolds-averaged Navier-Stokes equation to determine Eulerian droplet flow. The results demonstrate the ability of the software to estimate pressure coefficient, collection efficiency, and rime ice shape, indicating its potential use in icing simulations. Furthermore, the paper investigates the effect of different numerical schemes, linear solvers, and turbulence models on the numerical results. The rime ice occurs only through accretion, excluding thermodynamic processes, accounting for ice growth effects with the immersed boundary method. The results exhibited consistency with the NASA experiments.

1. Introduction

To certify an aircraft for in-flight icing encounters, the first step is to perform an impingement analysis. This involves calculating the collection efficiency (β), which represents the water concentration around the body. These calculations help estimate the ice accumulation on the aircraft's exposed surfaces during its passage through supercooled droplet clouds. The next stage involves simulating glaze ice at key locations, followed by predicting the shapes of rime ice.

Once these ice formations are modeled, an aerodynamic evaluation is required to assess their impact on aircraft operations and safety. Consequently, CFD and ice simulations, along with wind and icing tunnel tests, are essential for aircraft certification.

THE ROYAL SOCIETY PUBLISHING

(a) 3D Ice Codes

In terms of three-dimensional icing simulations, NASA's LEWICE3D (1) stands out as a pioneer code that addresses 3D icing phenomena. This code integrates flow solutions obtained from external CFD and determines droplet paths using a Lagrangian approach. Although the flow solutions and impingement are 3D, the water film is modeled using a two-dimensional approach, considering normal slices along the wing.

Similarly to the water model, the thermodynamics and growth of ice are also calculated within two-dimensional slices. This approach is called a quasi-3D solution to the ice-accretion problem. Instead of following the shear lines, the code makes several normal cuts to the wing to solve the water film and the ice accretion. Depending on the sweep angle, the shear lines form an accentuated curve after stagnation and depart significantly from the normal direction cut made by LEWICE3D (1).

The FENSAP code (2), originally developed by the Habashi team at McGill University, uses a 3D CFD flow solution and calculates droplet trajectories using an Eulerian formulation. In addition to the impingement module, the FENSAP code also includes modules for heat transfer and ice growth. These three droplet modules, along with the CFD flow equations, were solved iteratively to calculate the final shape of the ice.

ONERA developed a 3D code for the prediction of ice shape over several years. One of the first versions is from Hedde and Guffond (3), followed by others, such as IGLOO3D by Radenac and Duchayne (4). Additional developments included the incorporation of the effect of ice crystals (5), the use of the integral boundary layer (6), and the application of the immersed boundary method (7).

Other examples include the PoliMIce code (8) from Politecnico di Milano, and several CIRA codes (9; 10) that were developed for specific applications. The Embraer Aircraft Company also has several codes, some of which have been published by Martins da Silva (11), alongside contributions from other research groups worldwide (12; 13; 14; 15).

Several attempts have been made to simulate quasi-3D ice shape formation, such as the separated 2D simulations by Martins da Silva et al. (11) and the normal cuts to the leading edge in the original LEWICE3D code by Bidwell (1). These simulations account for the pressure distribution and impingement of the 3D simulation while performing the runback flow, heat transfer, thermal balance, and ice growth along a line normal to the leading edge.

In terms of approval by regulatory authorities, no 3D code has yet gained widespread acceptance, but they are accepted since each company validated them during the certification. On the other hand, 2D codes have earned recognition and acceptance for certain applications, especially on wings and airfoils. This limited acceptance of 3D codes is primarily due to the fact that the technology for simulating 3D ice accretion is not yet fully developed. For example, no code can replicate the glaze ice lobster tail formation on the swept wings.

The present paper introduces a new foam-ext. based code, iceAccretionFoam, that has a different characteristic of adopting the advanced immersed boundary method of Jasak (16). In addition, it is an initial framework that can be extended in the future with the adoption of the finite-area method for the runback liquid water flow in all regimes, including film, rivulets, and beads. Future versions of the code could also integrate the rough wall functions validated by Lima da Silva et al. (17), using a modified Stefanini correlation (18), and a laminar-transition model triggered by roughness in a compressible solver with the energy equation.

(b) OpenFoam applied to Aircraft Icing

Beld (19) employed OpenFOAM's reactingParcelFilmFoam solver, which is a water film solution but it is not based on finite area, to model droplet impingement and film layer formation on aircraft bodies, using Lagrangian particle tracking to define particle paths in the simulation. Particles are injected upstream and their paths, influenced by drag and gravitational forces, are computed to create a surface film layer.

Li et al. (20) introduced a method to simulate ice accretion on an aircraft wing by integrating a three-dimensional compressible Navier-Stokes solver, an Eulerian droplet flow field model, a mesh morphing model but not an immersed boundary, and a thermodynamic model. All of these were implemented in OpenFOAM. The Eulerian two-phase model is used in the droplet motion solver, which couples with the

airflow solver, considering droplets in the airflow. The droplet collection efficiency is determined by solving these equations, and a specific impingement boundary condition and a roughness wall function of da Silva et al. (17) effectively help simulate the phenomenon of icing. Results for the three-dimensional Onera M6 wing configuration were demonstrated; however, experimental validation was not conducted.

Berberovic et al. (21) modeled the formation of ice using a phase field approach, capturing the dynamics of the ice-water interface and incorporating thermal effects. Both rime and glaze ice formations are considered, with an emphasis on the solidification of supercooled water. The results demonstrate the model's capability to predict the solidification process of supercooled water, validated against theoretical results for ice-dendrite growth.

Furthermore, de Rosa et al. (22) employed a thorough approach using the Messinger model to simulate the formation of rime and glaze ice. This study differentiated between various icing conditions based on the equilibrium temperature of the wall and the freezing fraction, enabling the simulation of running-wet, rime ice, and glaze-ice scenarios. Ice growth was modeled using the immersed boundary method on a three-dimensional Cartesian grid. The study showed satisfactory agreement with the experimental data on the accretion limits and average ice thickness.

In addition, Paz et al. (23) implemented ice formation modeling using 3D Immersed Boundary Methods (IBM) to calculate droplet trajectories. The methodology revolves around a multistep approach, adapting the fluid volume mesh in response to ice accretion, thereby handling complex ice shapes and automating the simulation process. The results of the study are deemed satisfactory on the basis of good agreement with the solutions. The authors highlight the effectiveness of the IBM approach in ice formation simulations, particularly in handling complex geometries under compressible subsonic conditions, as demonstrated in cases involving an iced GLC305 airfoil and a sphere.

(c) Objective

The objective of this paper is to delineate the initial advancements in the development of a three-dimensional (3D) ice accretion simulation employing Foam-extend 5.0 for rime ice shape prediction. The code employs the Unsteady Reynolds-Averaged Navier-Stokes (URANS), an Eulerian droplet impingement plus the application of the immersed boundary method to grow the ice surface. The authors implemented a validation process for the results of the pressure coefficient, collection efficiency, and ice shape geometry. Furthermore, the study considered three different models of ice density, and examined variations in upwind numerical schemes, turbulence models, and pressure linear solvers.

2. Mathematical Models

(a) Main Air Flow

The PIMPLE algorithm is used in computational fluid dynamics for transient analyses. It combines the SIMPLE algorithm (24) with the PISO algorithm (25). This technique is intended to provide efficient solutions to fluid dynamics problems, particularly in scenarios with unsteady flows, large time increments, or significant velocity-pressure coupling. The following equations for the primary airflow can be found in Jasak (26):

$$\frac{\partial \mathbf{U}}{\partial t} + \nabla \cdot (\mathbf{U}\mathbf{U}) - \nu \nabla^2 \mathbf{U} = -\nabla p \tag{2.1}$$

$$\nabla^2 p = \nabla \cdot \mathbf{H}(\mathbf{U}) \quad \text{where} \quad \mathbf{H}(\mathbf{U}) = -\nabla \cdot (\mathbf{U}\mathbf{U}) \tag{2.2}$$

(b) Dispersed Phase Flow

The iceAccretionFoam uses drift flux modeling to represent distinct phases as a mixture phase. The incompressible dispersed phase, denoted by $U_{phase,i}$ and α_i, is computed using the driftFlux model. Each

droplet size, indexed by i from 1 to the maximum number of diameters, is treated as an individual phase in the distribution.

$$\left\|\vec{U}_{rel,i}\right\| = \left\|\vec{U}_{phase,i} - \vec{U}\right\| \tag{2.3}$$

$$Re_{rel,i} = \max\left(2.4,\ \left\|\vec{U}_{rel,i}\right\| \cdot \frac{d_i}{\nu_D}\right) \tag{2.4}$$

$$C_{d,i} = \max\left[0.5,\ \frac{24}{Re_{rel,i}}\left(1 + 0.15 \cdot Re_{rel,i}^{0.687}\right)\right] \tag{2.5}$$

$$DragPf_i = \frac{3}{4} \cdot C_{d,i} \cdot \frac{\rho_C}{\rho_D} \cdot \frac{\left\|\vec{U}_{rel,i}\right\|}{d_i} \tag{2.6}$$

$$\begin{aligned} &\frac{\partial \tilde{\mathbf{U}}_{\mathbf{phase,i}}}{\partial t} + \nabla \cdot (\vec{\boldsymbol{\phi}}_{\boldsymbol{cont_i}} \cdot \tilde{\mathbf{U}}_{\mathbf{phase,i}}) = \\ &\mathbf{g} + DragPf_i(\tilde{\mathbf{U}}_{\mathbf{rel,i}}) - \frac{3}{4} C_{d,i} \cdot \left\|\vec{U}_{rel,i}\right\| \cdot \nu_t \cdot \frac{\nabla \alpha_i}{d} \end{aligned} \tag{2.7}$$

Here, ϕ_{cont} is the flux of the continuous phase or the main flow. The equation for α, volumetric fraction, is listed below:

$$\frac{\partial \alpha_i}{\partial t} + \nabla \cdot (\tilde{\phi}_{\mathbf{phase_i}} \cdot \alpha_i) = 0 \tag{2.8}$$

Here, ϕ_{phase} is the flux of the droplet phase or the flow of the dispersed phase.

(c) Ice Growth Modeling

Using equations 2.9 and 2.10, the height of the ice, h_{ice}, on the surface impacted by water droplets can be determined considering the contribution of the combined parcel from each phase i at the end of $\Delta t_{accretion}$:

$$h_{ice,i} = \Delta t_{accretion} \cdot \alpha_i \cdot U_{phase,i} \cdot \frac{\rho_{water}}{\rho_{ice}} \tag{2.9}$$

$$h_{ice} = \sum_{i=1}^{n} h_{ice,i} \tag{2.10}$$

At the end of the $\Delta t_{accretion}$ cycle, $h_{ice,j}$ is summed with the previous value of $h_{ice,j-1}$. The simulation starts with $h_{ice,0} = 0$. The present authors used 12 steps of 30 s to simulate 360 s of icing time, so $1 \leq j \leq 12$. However, the simulation continued until the 13^{th} step because ice growth occurs 0.5 seconds after the 1 s flow solution. The deformed field, which represents the height of the ice (h_{ice}), is used to modify the computational domain of the immersed boundary. A minimum threshold for boundary movement is established to determine when the boundary should be updated. The height is used to move the boundary normally to the surface at each face of the surface mesh.

The process of ice growth can be fully simulated in a transient manner, which means that ice accretion occurs at each time step of the flow solution. Alternatively, to simulate the ice formation process in steps, the time interval for the flow solution (Δt_{flow}) can be shorter than the time interval for the ice accretion ($\Delta t_{accretion}$). Thus, the total time for accretion can be divided into $nt = t_{total}/\Delta t_{accretion}$ steps, with a flow solution of Δt_{flow} between each step. The user can arbitrarily choose the values of Δt_{flow} and $\Delta t_{accretion}$ to maintain accuracy while simultaneously accelerating the solution. In this multistep solution

condition for ice growth, it is assumed that the collection efficiency remains relatively constant for the defined time interval $\Delta t_{accretion}$.

(d) Ice Density

This study investigated three ice density models: LEWICE (27); Jones (28); and Macklin (29). The density of ice is influenced by the quantity of air trapped during its formation and therefore depends on factors such as the median volumetric diameter, liquid water content, size of the body, freestream velocity, and recovery temperature of the surface. The trapped air decreases the density of the rime ice, giving it an opaque look. Glaze ice, on the contrary, has increased density as a result of a denser structure with minimal air, making it more transparent.

For LEWICE (27):

$$\rho_{ice} = 1000 \cdot \exp\left[0.15 \cdot \left(1 + 6043 \cdot S^{-2.65}\right)\right] \tag{2.11}$$

$$S = \frac{\text{MVD}^{0.82} \cdot U_{\infty}^{0.59} \cdot \text{LWC}^{0.21}}{d_{le}^{0.48} \cdot (-T_{rec}^{0.23})} \tag{2.12}$$

For Jones (28):

$$\rho_{ice} = \begin{cases} 0.210 \cdot R^{0.53} & \text{for } R \leq 10 \\ \dfrac{R}{1.15 \cdot R + 2.94} & \text{for } 10 < R < 60 \\ 0.84 & \text{for } R \geq 60 \end{cases} \tag{2.13}$$

where R is the Macklin parameter $-d_{le} \times U_{\infty}/(2T_{rec})$, where d_{le} is the diameter of the leading edge, U_{∞} is the freestream velocity, T_{rec} is in Celsius, thus, a negative value and lower than zero.

For Macklin (29):

$$\rho_{ice} = \begin{cases} 0.110 \cdot R^{0.76} & \text{for } R \leq 17 \\ 0.9 & \text{for } R > 17 \end{cases} \tag{2.14}$$

The only local parameter considered is the recovery temperature T_{rec}, which varies along the surface and depends on the local Mach number (M) that depends on the local pressure values.

$$T_{\text{rec}} = T_{\infty} \cdot \left(1 + r \cdot \frac{\gamma - 1}{2} \cdot M_{\text{local}}^2\right) \tag{2.15}$$

$$M_{\text{local}} = \sqrt{\frac{2}{\gamma - 1}\left[\left(\frac{P_{\text{local}}}{P_{total,\infty}}\right)^{-\frac{\gamma-1}{\gamma}} - 1\right]} \tag{2.16}$$

where $r = \text{Pr}^{1/3}$ for turbulent flows and $\gamma = 1.4$ for air. If the solver had compressibility capability and solved the energy equation, the simulation would yield the value of T_{rec} due to the effects of compression and kinetic heating caused by viscosity. In the current model, the flow equations are assumed to be incompressible, and the energy equation is not solved; therefore, the Eq. (2.15) is required. This is only an initial approach to allow for the calculation of ice density.

3. Methodology

(a) IceAccretionFoam Description

The Foam-extend 5.0 numerical simulation library is a fork of the original Foam code (30), developed by Jasak and Weller at Imperial College in the 1990s (31; 32). The authors of the present paper are developing

a new tool, named iceAccretionFoam, which incorporates standard foam-extend features, such as the finite-area water model and the immersed boundary method.

A single 3D CFD code is all that is needed for all calculations. It is worth noting that this initial tool is currently suitable only for the rime ice regime; however, the framework is designed to include all components necessary for the development of mixed and glaze ice. Future work will involve integrating convective heat transfer (17; 18) with transition (33; 34), solidification process, and the dynamics of water at the interface by applying the finite-area technique (35) and leveraging previous experience (36).

The iceAccretionFoam solver for rime ice accretion, as delineated in this manuscript, exhibits the following distinctive attributes.

(i) A transient flow solution using URANS incompressible equations with a time step Δt_{flow} for the flow and a larger time step $\Delta t_{accretion}$ for ice growth, simulating the process as multi-step;
(ii) An immersed boundary method (37) that updates the solid surface boundary and redefines the mesh around the new surface created by growth;
(iii) The capability to incorporate a user-defined droplet distribution (38; 39) with n bins, based on the median volumetric diameter (MVD) and the fraction of the freestream liquid water content (FLWC);
(iv) An implementation of the Langmuir-D-type distribution (40), incorporating a 7-bin diameter and the fraction of the FLWC, contingent upon the provision of an MVD by the user;
(v) An Eulerian-dispersed phase model adapted from the extant driftEulerFoam solver, where each droplet diameter is treated as a distinct phase, characterized by the volumetric water fraction α and the phase velocity U_{phase}.

To ensure that the problem aligns with the rime ice shape simulation for the current analysis, the following assumptions are made: a) All impinging water instantaneously solidifies upon contact; b) A normal ice growth rule is applied to all surfaces subjected to impingement; c) Thermal balance and convective heat and mass transfer calculations are not performed, as they are unnecessary for simple rime ice accretion in the context of this study; d) Liquid water is assumed to be absent on the airfoil surface; e) The airfoil surface is considered to be adiabatic; f) Thermal conduction within the airfoil surface is neglected; g) Phenomena such as splashing, re-impingement, and other secondary effects associated with Super Large Droplets (SLD) are disregarded; h) The droplet is modeled as a perfect sphere, and the drag correlation omits deformation effects; i) The droplet weight is not considered. These assumptions will change according to the evolution of the iceAccretionFoam code, for example, when simulating the glaze ice shape, SLD, or thermal ice protection system in future versions.

(b) Numerical Model for Ice Growth

Numerical modeling in ice accretion simulations must account for substantial changes in the geometry of the flow domain due to ice accretion on solid walls. To handle this, the Immersed Boundary Surface Method (37) is applied, where the body-fitted fixed polyhedral background mesh is modified using a deforming immersed triangular surface. The interaction between the immersed surface and the background mesh is developed in the spirit of immersed boundary solvers.

Jasak introduced an enhanced version of IBM, termed the Immersed Boundary Surface Method (IBS), as referenced in (16). This approach is formulated to handle the immersed geometry within the background mesh in a manner resembling a body-fitted mesh, thereby preserving the topology of both the background and surface meshes. This method deviates from the traditional cut-cell strategy. Figure 1 demonstrates the application of IBS by partitioning three cells into segments. These segmented cells, composed of active and inactive portions, undergo an adjustment in their discretization matrix while maintaining their inherent topology. Modifications pertain to the cell center, area, and volume based on the active segments. This adjusted matrix incorporates the boundary conditions of the immersed geometry into the background mesh through the resultant IB-surface.

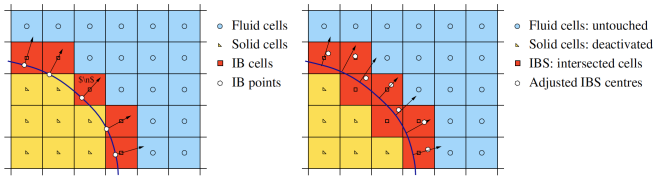

Figure 1: Traditional IBM and New Implementation of IBS after Jasak (16).

(c) Strategy for Validation

Validation involves assessing the classical rime ice formation on the NACA0012 airfoil profile, as described by Shin and Bond (41). This is further supported by airfoil data for C_p on the NACA0012 profile (42) and numerical results from LEWICE2D simulations for parameter β (43).

The use of the NACA0012 airfoil limits the validation of impingement and β, as it is based on simulated data from Al-Khalil et al.(43) rather than experimental data, although the numerical results are derived from the traditional LEWICE2D code. It is crucial to acknowledge that the validation of rime ice formation and pressure coefficients relied on conventionally reliable experimental data sets. The authors gave precedence to the Shin and Bond ice configuration dataset (44; 45), which used the NACA0012 airfoil. A possible agreement of the pressure coefficient C_p usually suggests that the results of β are acceptable for a simple airfoil analysis. Given that this paper offers preliminary validation, subsequent research will focus on airfoils, incorporating experimental β datasets from other sources, such as those published by Papadakis et al. (39).

4. Simulation Configuration

(a) Solver Setup

The Preconditioned Conjugate Gradient (PCG) method is widely preferred for its efficiency in solving symmetric positive definite matrices, making it suitable for aerodynamic simulations with extensive and sparse matrix systems (46). However, in highly complex scenarios, its accuracy may be slightly compromised. On the other hand, the Algebraic Multigrid (AMG) solver is acclaimed for its robustness and scalability, making it highly effective for addressing intricate aerodynamic challenges with fluctuating coefficients. It achieves an optimal balance between computational speed and precision (47). The Geometric Algebraic Multigrid (GAMG) solver, combining geometric and algebraic approaches, offers enhanced accuracy for large-scale aerodynamic projects. However, this comes at the cost of potentially higher computational requirements compared to PCG (48).

Accurate Management of discontinuities in the water concentration field, α, is a critical aspect of aerodynamic simulations, particularly when employing Total Variation Diminishing (TVD) schemes. The Limited Upwind Scheme for Transport (LUST) has proven effective in reducing numerical diffusion, a critical factor for the precise delineation of shadow zones and for the prevention of synthetic concentration peaks at stagnation points. By blending first-order and second-order schemes, LUST effectively balances accuracy and stability in aerodynamic simulations (49). The Monotonic Upstream-Centered Scheme for Conservation Laws (MUSCL) enhances the Godunov scheme to achieve superior resolution of steep gradients, thereby preserving the integrity of discontinuities in α while preventing the occurrence of false oscillations (50). Performing well in the management of flow discontinuities, the Van Leer scheme demonstrates particular proficiency in regulating variations of the concentration field near stagnation points (51). The MINMOD limiter (Minimum Modulus) preserves monotonicity and effectively prevents the formation of nonphysical concentration peaks in complex flow domains (52). Furthermore, the Second-Order Upwind Scheme, by assimilating downstream information, improves the accuracy in depicting α across discontinuities, which proves advantageous for the prediction of concentration fields in aerodynamic flows (53).

The $k-\epsilon$ realizable model provides improvements, especially in predicting the spread rate of jets and flows that involve rotation and boundary layers under strong adverse pressure gradients, making it more suitable for complex aerodynamic applications (44). The $k-\omega$ SST model is highly respected in aerodynamics, particularly for its ability to accurately capture the effects of the boundary layer due to its formulation, which blends the behavior of $k-\omega$ in the region near the wall with $k-\epsilon$ in the far field (54). The Spalart-Almaras turbulence model (55) is a one-equation model specifically designed for aerospace applications. It excels in wall-bounded flows and adverse pressure gradient scenarios. Being a low Reynolds number model, it does not use wall functions, making it suitable for near-wall turbulence.

(b) Numerical Setup

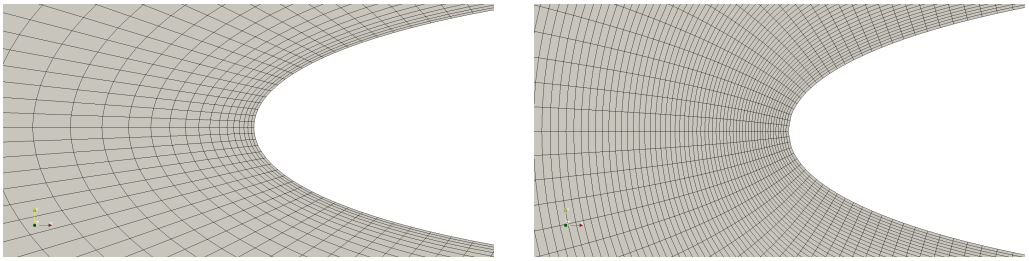

(a) Coarse Mesh. (b) Fine Mesh.

Figure 2: Meshes used for β and C_p simulations.

The mesh used in this study is composed of O-Type, structured, and hexahedral elements, notably excluding any prism layers. The coarse mesh consists of approximately 7,000 elements, with the leading edge shown in Figure 2a, while the fine mesh comprises around 66,000 elements, as shown in Figure 2b. An overview of the mesh is presented in Figure 3; the same domain size is adopted for the coarse mesh. The absence of prism layers is intentional, as simulation of impingement and rime ice accretion does not necessitate a highly accurate viscous-flow solution for heat transfer or friction. Consequently, a simplified flow solution, such as the potential flow or Euler equations, is sufficient to resolve the flow characteristics without significant issues. However, the fine mesh is essential for offering higher resolution to the ice-growth formation because the present authors are using an approach involving the immersed boundary method.

Regarding boundary conditions, the pressure p exhibits a zero gradient freestream type at all external boundaries. The velocity U is specified as a freestream type with a fixed value. At the boundaries, the velocity U_{phase} matches U, with a zero gradient applied for incoming particles and a fixed zero value assigned to outgoing particles at the faces. The configuration of α on the surface is analogous to that of U_{phase} and is determined in the freestream using LWC through the relation:

$$\alpha_\infty = \frac{LWC_\infty}{\rho_{water}} \tag{4.1}$$

5. Results and Discussion

(a) Test Case Definition

In this study, three different distributions were used: a) the distribution used by Papadakis (39) in various studies carried out at NASA IRT, as shown in Table 1; b) the distribution utilized by Wright (38) to validate the LEWICE 3.0 software, detailed in Table 2; and c) the theoretical distribution of Langmuir-D, a widely cited distribution recognized by authorities (40; 56), as illustrated in Table 3.

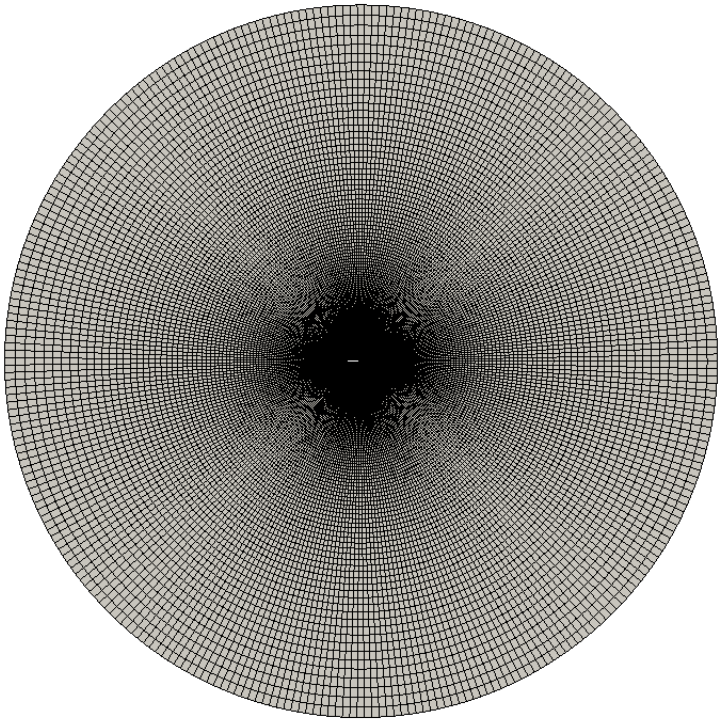

Figure 3: Fine Mesh overview with the body at the center.

Table 1: Discrete Cumulative Distribution of Papadakis (39) with MVD = 20 μm.

Cumulative % LWC	**% LWC**	**D(I) / MVD**	**D(I)**
97.5	5	0.2770	5.540
90.0	10	0.4460	8.920
75.0	20	0.6817	13.634
50.0	30	1.0000	20.000
25.0	20	1.5865	31.730
10.0	10	2.2943	45.886
2.5	5	3.2542	65.084

The pressure coefficient is computed along the surface by:

$$C_p = \frac{p - p_\infty}{\frac{1}{2}\rho U_\infty^2} \tag{5.1}$$

where p and p_∞ represent the pressure values in the local and far fields, respectively, while ρ is the density and U_∞ is the velocity in the far field. The experimental data C_p were derived from Emmons' NACA investigation (42), which was carried out under incompressibility conditions, specifically at Mach zero and an angle of attack (AOA) of 0°. Additionally, Drela's XFoil solver (57) was used to compare the results for AOA of 0°. Both Reynolds and Mach numbers were calculated on the basis of free-stream conditions, with the transition from laminar to turbulent flow occurring immediately after the stagnation point. This ensures that the C_p results are fully turbulent and take viscosity into account.

The collection efficiencies, β_i and β_{tot}, can be defined as follows:

Table 2: Distribution of Wright (38) with MVD = 21 μm.

% LWC	D(I)
0.1390	8.6
0.0958	12.5
0.0997	15.5
0.1220	18.5
0.1208	21.5
0.1115	24.5
0.0917	27.5
0.0946	31.6
0.0899	48.2
0.0350	95.9

Table 3: Theoretical Langmuir-D Distribution (40) with MVD = 20 μm.

% LWC	$(a/ao)^2$	D(I)
5	0.31	6.2
10	0.52	10.4
20	0.71	14.2
30	1.00	20.0
20	1.37	27.4
10	1.74	34.8
5	2.22	44.4

$$\beta_i = \frac{\alpha_i \cdot \vec{U}_{phase,i} \cdot \vec{n}}{\alpha_\infty \cdot |\vec{U}_{phase,\infty}|} \tag{5.2}$$

$$\beta_{tot} = \sum_{i=1}^{n} \frac{\alpha_i \cdot \beta_i}{\alpha_\infty} \tag{5.3}$$

$$\alpha_\infty = \sum_{i=1}^{n} \alpha_i \tag{5.4}$$

where i is the phase and n is the number of phases. The values of α_∞ and each α_i are defined in Tables 1, 2 and 3. The β_{tot} is determined by weighting the values of β_i by α_i, as shown in Eq. 5.3.

As a test case for the formation of rime ice, the present authors selected a case from the Shin and Bond dataset (41; 45). The case is a rime formation on the test body with a static temperature (T_∞) of -15 °F (247.04 K), an MVD of 20 μm, a LWC of 1.0 g/m^3 and a U_∞ of 150 mph (67 m/s). They conducted their experiments using a NACA0012 airfoil with a chord of 0.53 m at an AOA of 4° . They measured the accretion shape at 360 s for this specific case. The authors of the present study adopted a pressure altitude of 2,000 feet (approximately 610 m above sea level) since the pressure in the test section was not defined by the owners of the experimental dataset.

(b) Numerical Results

The present paper shows three types of results: pressure coefficient, collection efficiency, and rime ice shape. The accuracy of the predicted rime ice shape is strongly influenced by the efficiency of droplet collection as well as the distribution of water concentration. Furthermore, the collection efficiency is directly dependent

on the pressure coefficient and the velocities normal to the airfoil surface. This dependency is why this paper not only presents the rime ice shapes but also includes the results of C_p and β as part of a validation process for the NACA0012 airfoil.

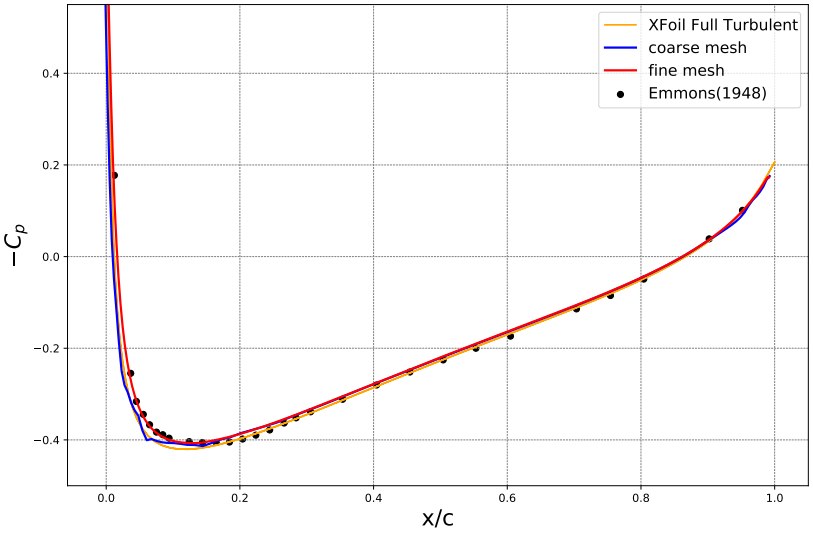

Figure 4: C_p distributions at 0° AOA. AMG solver and $k-\epsilon$ turbulence model.

Figure 4 illustrates the negative pressure coefficient ($-C_p$) along the chord length of a NACA0012 airfoil at a 0° AOA. The x/c is the axial distance from the geometrical leading edge located at the minimum X coordinate of the airfoil. The results of the present study are compared with the Emmons' experimental data (42) and the Xfoil results (57), obtained through simulations under incompressible flow conditions with $\mathrm{M} = 0.2$ and $\mathrm{Re} = 4.6E6$. The full turbulent simulation in Xfoil is ensured by fixing the transition immediately after the stagnation point.

Despite the fact that XFoil uses a Kármán-Tsien (58) correction for C_p, the current authors employed the Prandtl-Glauert (59) transformation in conjunction with the GAMG, AMG and PCG solvers as delineated below. This would not affect the correction since the Mach number is outside the compressible and far from the transonic regime.

$$C_p^* = C_p \cdot \frac{1}{\sqrt{1 - M_\infty^2}} \tag{5.5}$$

where M_∞ is the Mach number in the freestream. This correction helps the computational results to be close to Emmons' experimental data (42), particularly evident in the low-pressure peak near the leading edge, which is the region most important for ice formation.

Upon comparing the coarse mesh with the fine mesh, it becomes evident that the fine mesh exhibits a closer adherence to experimental data compared to both XFoil and the coarse mesh. Furthermore, the fine mesh yields a smoother solution, devoid of discontinuities, in contrast to the coarse mesh. This difference will lead to different impingement results for coarse and fine meshes.

The consistent results from the GAMG, AMG and PCG solvers for C_p (Figure 4) and impingement β (Figure 5) over the airfoil are likely due to the simplicity of the flow conditions, since there is no recirculation, complex geometry, or separation bubbles. These solvers converge to the same solution because the problem is straightforward and well-posed, ensuring that the underlying physics is accurately captured without significant numerical challenges. However, this condition may change if the ice shape is large and nonuniform, as in the case of glaze ice.

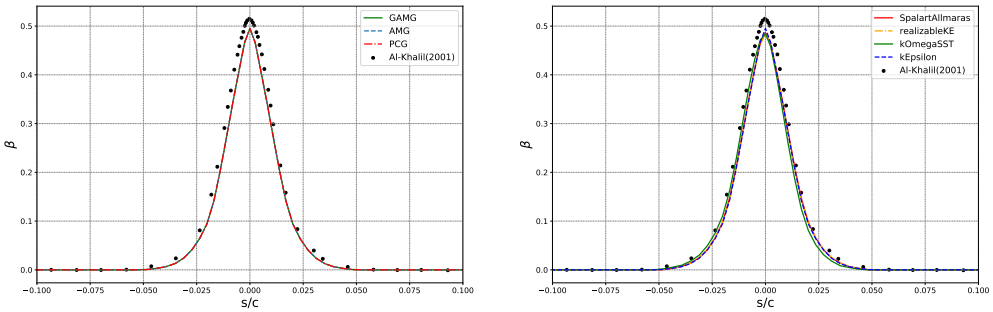

(a) Linear solvers. k-ϵ turbulence model.

(b) Turbulence models. AMG solver.

Figure 5: Langmuir-D (40) - coarse mesh - compared with Al-Khalil (43) simulation results with LEWICE2D (43).

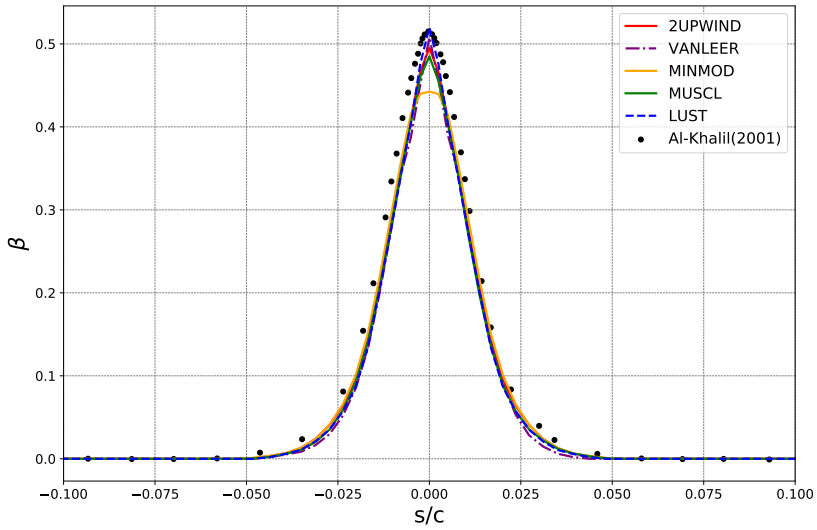

Figure 6: Langmuir-D (40). AMG solver. k-ϵ turbulence model - coarse mesh, TVD numerical schemes. Comparison with Al-Khalil simulation results with LEWICE2D (43).

The comparison of β values between the linear solvers and Al-Khalil's experimental data is depicted in Figure 5a within the streamwise airfoil region. Here, s/c represents the streamwise distance on the airfoil surface measured from the geometrical leading edge, which is located at the minimum X coordinate of the airfoil. Upstream of the leading edge, the distributions align well with the experimental data. The linear solvers' results are very similar when comparing the peak values, the area under the β curve, and the average values.

By varying the turbulence models, the results of the numerical distribution of β are compared with the experimental data of Al-Khalil in Figure 5b. The growth of the β values in all numerical solutions exhibits a slight delay in comparison to the experimental results ($-0.05 < S/C < -0.01$) and a premature decrease in the region between $0.02 < S/C < 0.05$. In the peak region, see Figure 5b, the $k - \epsilon$ is the model closest to the correct value.

The accuracy of turbulence models in the near-wall region is critical as it directly impacts the formation of glaze ice, which forms when supercooled water droplets freeze after impact in the runback water, heavily

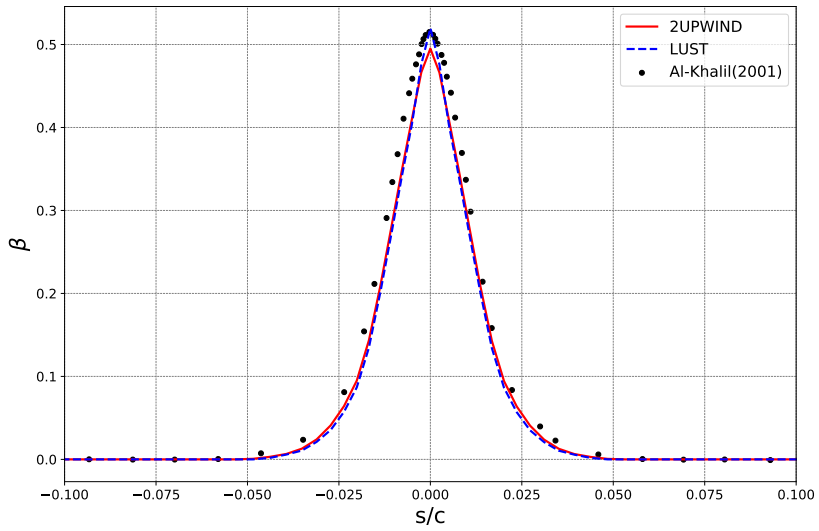

Figure 7: Langmuir-D (40). AMG solver. k-ϵ turbulence model - coarse mesh, TVD LUST vs. second-order upwind. Comparison with Al-Khalil simulation results with LEWICE2D (43).

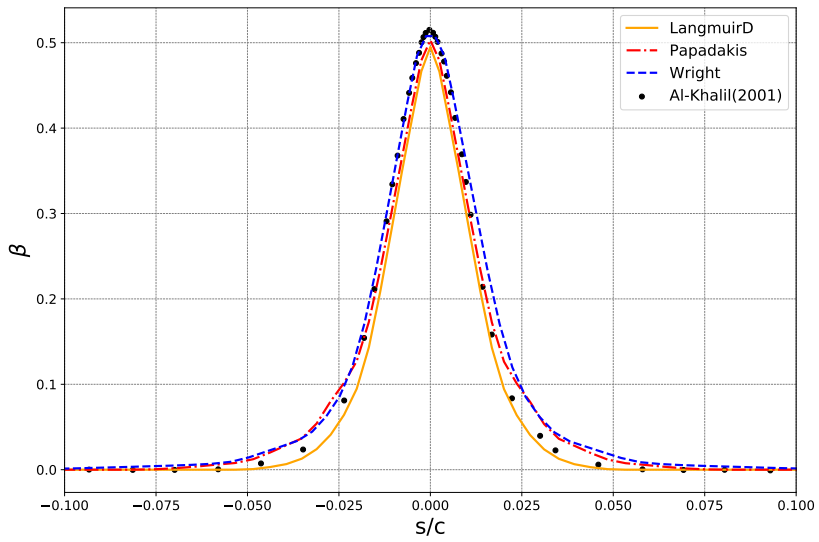

Figure 8: Langmuir-D (40). AMG solver. k-ϵ turbulence model. TVD second-order upwind - coarse mesh. Comparison with Al-Khalil simulation results with LEWICE2D (43).

influenced by heat transfer rates. However, rime ice accretion, which is presented in the present paper, involves a dry growth of ice without a thermal balance calculation because it forms instantly as supercooled droplets at impact on the airfoil surface. Thus, the precision of turbulence models in the near-wall region is not as critical for rime ice accretion as it is for glaze ice accretion. Moreover, the investigation of turbulence conducted in this study seeks to assess the impact of each model on β. Based on the findings, it can be concluded that the turbulence model influences the peak of β and the decay of the β curve close to the impingement limits.

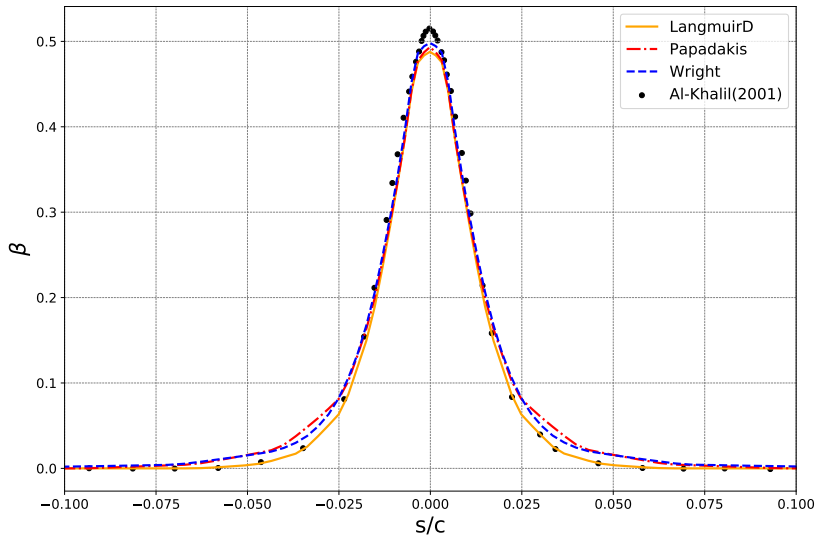

Figure 9: Langmuir-D (40). AMG solver. k-ϵ turbulence model. TVD second-order upwind - fine mesh. Comparison with Al-Khalil simulation results with LEWICE2D (43).

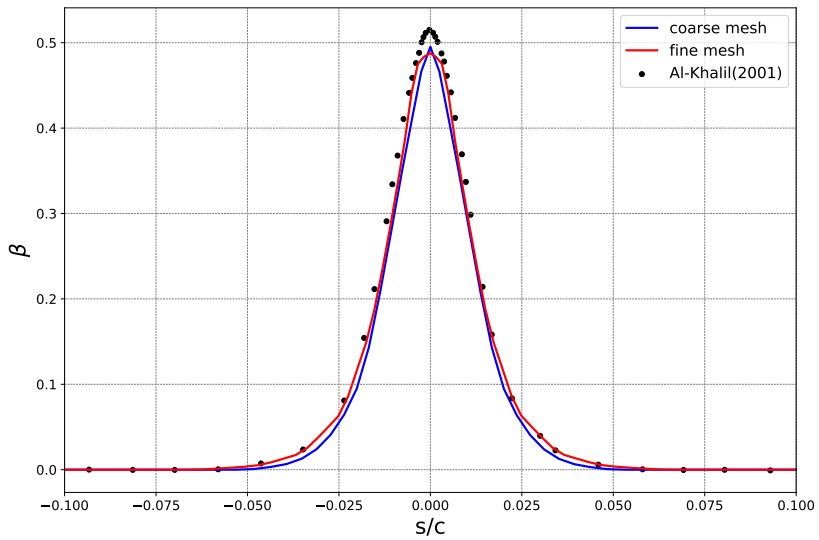

Figure 10: Langmuir-D (40). AMG solver. k-ϵ turbulence model. TVD second-order upwind - coarse and fine meshes comparison.Comparison with Al-Khalil simulation results with LEWICE2D (43).

In Figure 6, a comparison of β distributions is presented involving TVD schemes, including LUST, MUSCL, VANLEER, MINMOD, and Second-Order Upwind. The distributions align well in the region prior to the leading edge. As can be seen in Figure 7, the LUST result shows a close approximation to the experimental result right at the tip of the leading edge, but exhibits lower values for the remaining downstream regions. The Second-Order Upwind closely approximates the experimental data further downstream from the peak, but at the peak, it performs worse than LUST yet better than other models. In integral terms, Second-Order Upwind resulted in a close calculation relative to Al-Khalil's β simulations.

Figures 8 and 9 illustrate three simulated droplet distributions: the 20 μm MVD of Langmuir-D (40), the 20 μm MVD of Papadakis (39) and the 21 μm MVD of Wright (38), for coarse and fine mesh, respectively. It is apparent from both plots that the current model employing Langmuir-D in both meshes exhibits a closer alignment with Al-Khalil's LEWICE simulations (43) than the present model using other distributions. This observation suggests that Al-Khalil employed Langmuir-D as the distribution for the simulations. Furthermore, it can be inferred that the β calculated with Langmuir-D may not accurately represent the actual NASA icing tunnel, since the experimental distributions of Wright (38) and Papadakis (39) exhibit a higher deviation for β in the region just upstream of the impingement limits compared to the Langmuir-D distribution. Visually, it can be concluded that the simulation with fine mesh produced a β close to the Al-Khalil simulations for all distributions.

The authors also performed a simulation of β for two different meshes, coarse with 7,000 elements and fine with 66,000 elements. And also two other droplet size distributions: Wright (38) and Papadakis (39), both based in the Icing Research Tunnel of the Glenn Research Center. Figure 10 shows that the fine mesh has an improved result to replicate the numerical results of Al-Khalil (43) compared to the coarse mesh near the peak and downstream regions. This mesh certainly provides better results with respect to ice accretion and growth, as mentioned before. However, the Al-Khalil LEWICE results (43) may not reflect the actual conditions more accurately, as the ice formations predicted by the present model exhibit a closer alignment with the experimental data compared to the LEWICE simulation by Shin and Bond (44). At stagnation, the reduced values in β do not indicate a decreased ice accretion or a significant deviation in the ice shape at stagnation. Since there are no experimental data available for β in the NACA0012 airfoil, it is hard to state that the current model has larger deviations at stagnation. It can also be inferred that the integral under the β curve, which represents the quantity of impinged water, likely provides an accurate representation of the actual scenario, since the ice shape size predicted by the present model closely aligns with the experimental observations.

With regard to mass, the simulation provides an estimate that is sufficiently accurate, as the numerically simulated results from this paper closely align with those obtained by Al-Kalil et al. (43). At this stage of code development, an exact comparison of the integral of β is not essential.

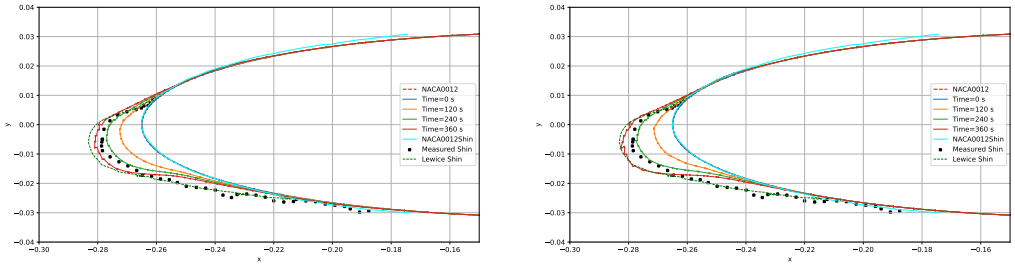

(a) Distribution of Papadakis (39).

(b) Distribution of Langmuir-D (40).

Figure 11: AMG solver. k-ϵ turbulence model. LEWICE ice density model (27). TVD second-order upwind - coarse mesh.

After testing C_p and β for various numerical schemes, the AMG linear solver for pressure, the $k-\epsilon$ turbulence model, and the Second Order Upwind TVD scheme were used for the rime ice growth simulations. The LUST scheme was also tested to compare the results with the Second-Order Upwind. The duration of the transient flow solution, Unsteady Reynolds Averaged Navier-Stokes (URANS), was set at 1 s, with ice growth occurring over 30 seconds in increments of 12 steps, reaching 360 s of ice accumulation.

It is important to note that, despite using the same airfoil, NACA0012, within a subsonic regime of a free-stream Mach number below 0.3, impingement calculations were performed at 0° AOA with a chord of 0.9144 m, while the prediction of rime ice accretion was performed at 4° AOA with a chord of 0.53

m. Furthermore, it should be noted that the parameter β varies with ice accretion at intervals of 30 seconds following an initial 1-second flow solution, in contrast to the impingement calculations, which use a constant β calculated at a 2-second flow solution period.

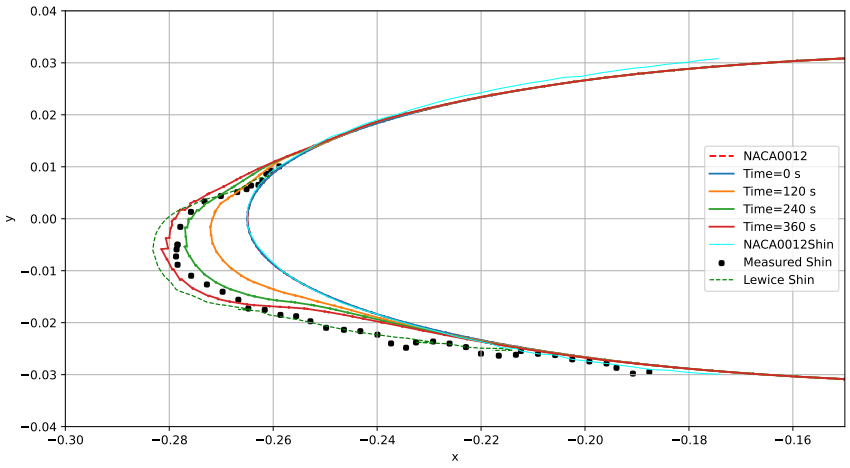

Figure 12: Distribution of Wright (38). AMG solver. k-ϵ turbulence model. LEWICE ice density model (27) and TVD second-order upwind - coarse mesh.

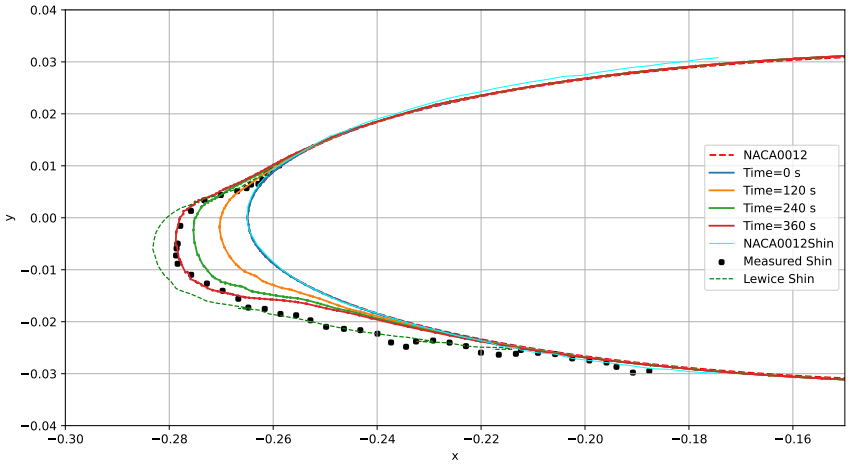

Figure 13: Distribution of Wright (38). AMG solver. k-ϵ turbulence model. LEWICE ice density model (27) and TVD second-order upwind - fine mesh.

Three different droplet distribution models were employed: a) theoretical Langmuir-D (40), b) experimental Wright (38), and c) experimental Papadakis (39). Furthermore, the authors contrasted the ice-shaped resemblance of coarse mesh with those of fine mesh. Lastly, the study highlighted the variations of the TVD Second-Order ice density and TVD LUST, as well as different correlations of the ice density with respect to ice growth and shape.

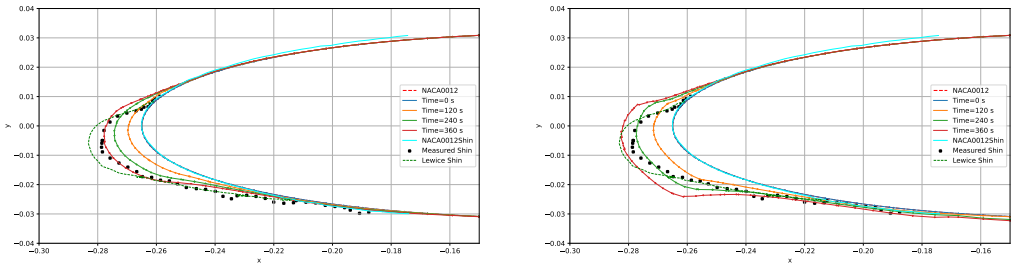

(a) Jones ice density (28).

(b) Macklin ice density (29).

Figure 14: Distribution of Wright (38). AMG solver. k-ϵ turbulence model. TVD second-order upwind - coarse mesh.

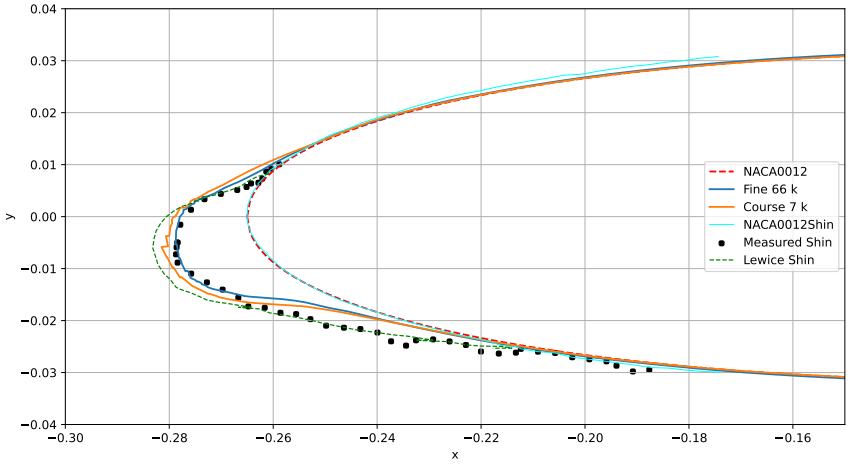

Figure 15: Distribution of Wright (38). AMG solver. k-ϵ turbulence model. LEWICE ice density model (27) - fine and coarse meshes, TVD second-order upwind.

Using Papadakis' icing tunnel distribution (Figure 11a) with LEWICE ice density, it is possible to note that the overall results tend to match Shin's base case (41; 45). At the end of the numerical simulation (time = 360 s), it becomes apparent that the numerical results slightly overestimate the shape of the ice, as observed in experiments.

The application of the LEWICE density model along with the Langmuir-D distribution did not successfully replicate the accurate ice shape shown in Figure 12. However, these results were close to the results of the Shin and Bond simulation with LEWICE (41; 45), demonstrating that LEWICE was executed using the Langmuir-D distribution.

Figures 12 and 13 illustrate the shapes of the rime ice computed using the Wright distribution (38), the LEWICE ice density model (27), and the TVD Second-Order Upwind.

In addition, Figure 12 shows the results obtained with a coarse mesh consisting of 7,000 elements, while Figure 13 shows the results obtained with a fine mesh containing 66,000 elements.

According to the results obtained using the Wright distribution in Figure 13 with LEWICE ice density, it should be noted that this model exhibited a closer approximation to the ice shape between all tested, making this configuration more suitable for the simulations of the ice shape. However, it also suggests

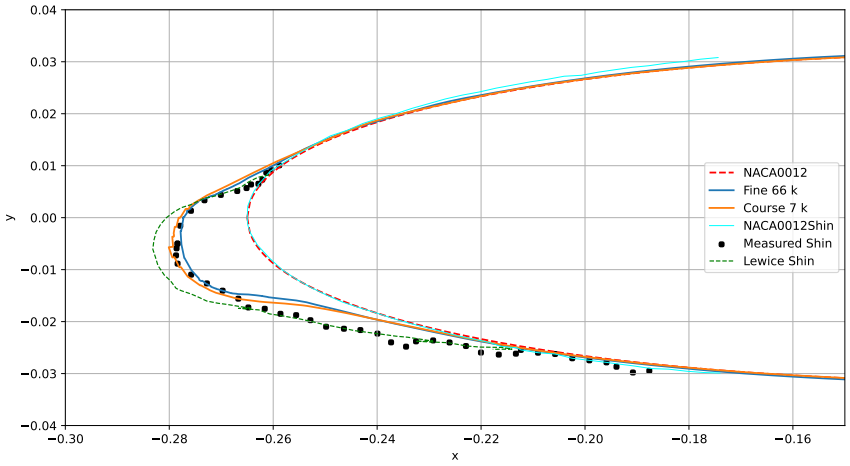

Figure 16: Distribution of Wright (38). AMG solver. k-ϵ turbulence model. LEWICE ice density model (27) - fine and coarse meshes, TVD LUST.

a discrepancy in the lower section, a feature shared by other models. This may point to the presence of a mixed-ice-type scenario, as the current code exclusively computes rime-ice formations. However, the results from the LEWICE code by Shin and Bond (41; 45) show better agreement with the experimental data, particularly in the lower section, than the current model. This is due to the consideration of a wet growth process or mixed ice accretion in LEWICE.

The results obtained using the Jones density model show greater deviation compared to the LEWICE model, as presented in Figure 14a. However, it is important to note that, in general, the Jones density model exhibited better accuracy than the Macklin ice density model with the same Wright distribution. Furthermore, the results obtained using the Macklin density model in Figure 14b proved to be the least favorable density model among the three models considered.

The influence of the two TVD schemes is shown in Figures 15 and 16. It is apparent that the TVD Second-Order Upwind scheme is slightly better than the LUST scheme on a fine mesh. While the LUST scheme aligns more closely with experimental data than Second-Order Upwind on a coarse mesh, it encounters convergence problems on a fine mesh.

6. Conclusions

This paper has introduced the initial development phase of a 3D ice accretion tool, built on foam-extend 5.0. This initial tool is designed to simulate the growth of the rime ice, incorporating features such as a transient flow solution, immersed boundary method, Eulerian-dispersed phase modeling, and user-defined droplet distributions.

The authors validated the results of C_p by comparing them with the findings of Emmons (42), assessed β against the research of Al-Khalil et al. (43) numerical simulation with LEWICE, and examined the shape of the rime ice according to a case study by Shin and Bond (41; 45). The analysis indicated a strong agreement between the simulated results and the experimental data.

The simulation of the present iceAccretionCode for rime ice produced results that closely matched the experimental data when considering a fine mesh, with 66,000 elements, the Wright (38) distribution, the AMG solver, the $k-\epsilon$ turbulence model, and the LEWICE ice density model (27). The same configuration produced satisfactory deviations for C_p and β compared to the experimental data and the LEWICE simulations, respectively.

The discrepancies observed in the results for TVD numerical schemes are more pronounced than those arising from variations in the turbulence models and linear solvers for the β simulations. Given that only TVD's have a significant impact on β and the shape of the rime ice is directly influenced by it, the investigation is confined to the variations in the shape of the ice that can be attributed to different TVD's. This observed invariance with respect to linear solvers and turbulence models may not hold when simulating glaze ice and more complex geometries.

It is essential to recognize that accurately simulating ice shape depends on the careful selection of the TVD scheme, a topic frequently overlooked or inadequately addressed in CFD Eulerian simulations. This difference is more significant at higher angles of attack than at lower angles due to the increase of the shadow zone.

This paper marks the first step towards developing a robust and comprehensive tool for 3D ice accretion simulation, with the ultimate goal of providing an accurate and accepted solution for aviation authorities.

References

1 Bidwell CS, Potapczuk MG. 1993 Users manual for the NASA Lewis three-dimensional ice accretion code (LEWICE 3D). Technical Memorandum NASA TM-105404 NASA Cleveland.

2 Beaugendre H, Morency F, Habashi WG. 2003 FENSAP-ICE's Three-Dimensional In-Flight Ice Accretion Module: ICE3D. *Journal of Aircraft* **40**, 239–247. (10.2514/2.3113)

3 Hedde T, Guffond D. 1995 ONERA Three-Dimensional Icing Model. *AIAA Journal* **33**, 1102–1108. (10.2514/3.12795)

4 Radenac E, Duchayne Q. 2022 IGLOO3D Simulations of the 1st AIAA Ice-Prediction Workshop Database. In *AIAA AVIATION 2022 Forum* pp. AIAA 2022–3310. (10.2514/6.2022-3310)

5 Laurent C, Bouyges M, Charton V, Bennani L, Senoner JM. 2022 Ice Crystals Accretion Capabilities of ONERA's 3D Icing Suite. In *AIAA AVIATION 2022 Forum* pp. AIAA 2022–3537. (10.2514/6.2022-3537)

6 Blanchard G, Radenac E, Bempedelis N, Bayeux C, Villedieu P. 2017 3D Ice Accretion Modeling Using an Integral Boundary Layer Method. In *7th European Conference for Aeronautics and Aerospace Sciences (EUCASS)*. (10.13009/EUCASS2017-400)

7 Lavoie P, Radenac E, Blanchard G, Laurendeau E, Villedieu P. 2022 Immersed boundary methodology for multistep ice accretion using a level set. *Journal of Aircraft* **59**, 912–926.

8 Gori G, Zocca M, Garabelli M, Guardone A, Quaranta G. 2015 PoliMIce: A simulation framework for three-dimensional ice accretion. *Applied Mathematics and Computation*. (10.1016/j.amc.2015.05.081)

9 Cinquegrana D, D'Aniello F, de Rosa D, Carozza A, Catalano P, Mingione G. 2023 A CIRA 3D Ice Accretion Code for Multiple Cloud Conditions Simulations. In *International Conference on Icing of Aircraft, Engines, and Structures*. SAE International. (10.4271/2023-01-1461)

10 Capizzano F, Catalano P, Carozza A, Cinquegrana D, Petrosino F. 2021 CIRA Icing Codes and Findings for the IPW Benchmarks. In *1st AIAA Ice Prediction Workshop*.

11 da Silva DM, Trapp LG, Domingos RH, Papa R, de Castro Santos LC. 2012 Quasi-3D Multi-Step Ice Accretion Simulation. In *50th AIAA Aerospace Sciences Meeting Including the New Horizons Forum and Aerospace Exposition* pp. AIAA 2012–0313. (10.2514/6.2012-0313)

12 Mu Z, Lin G, Bai L, Shen X, Bu X. 2017 3D Numerical Simulation of Ice Accretion on a Rotating Surface. *International Journal of Aeronautical & Space Sciences* **18**, 352–364. (10.5139/IJASS.2017.18.2.352)

13 Chang S, Tang H, Wu H, Su X, Lewis A, Ji C. 2018 Three-Dimensional Modelling and Simulation of the Ice Accretion Process on Aircraft Wings. *International Journal of Astronautics and Aeronautical Engineering* **3**, 1–25. (10.1016/j.ijaae.2018.020)

14 Jung S, Myong R. 2011 Efficient Prediction of Ice Shapes in CFD Simulation of In-Flight Icing Using a POD-Based Reduced Order Model. In *SAE International*. (10.2514/1.12345)

15 Jung S, Myong R. 2013 A Three-Dimensional Unstructured Finite Volume Method for Droplet Impingement in Aircraft Icing. In *21st AIAA Computational Fluid Dynamics Conference*. (10.2514/6.2013-2576)

16 Jasak H. 2018 Immersed Boundary Surface Method in Foam-Extend. In *The 13th OpenFOAM Workshop (OFW13)* pp. 55–59.

17 Silva GAL, Arima MN, Branco NN, Pimenta MM. 2011 Proposed Wall Function Models for Heat Transfer around a Cylinder with Rough Surface in Cross Flow. In *International Conference on Icing of Aircraft, Engines, and Structures* number 2011-38-0023 Chicago. (10.4271/2011-38-0023)
18 Stefanini LM, Silvares OM, Silva GAL, Zerbini EJGJ. 2010 Heat transfer on iced cylinders. In *AIAA Paper* number AIAA-2010-7672. (10.2514/6.2010-7672)
19 Beld EJ. 2013 Droplet impingement and film layer modeling as a basis for aircraft icing simulations in OpenFOAM. Master's thesis University of Twente.
20 Li S, Paoli R. 2019 Modeling of Ice Accretion over Aircraft Wings Using a Compressible OpenFOAM Solver. *International Journal of Aerospace Engineering* **2019**. Article ID 4864927 (10.1155/2019/4864927)
21 Berberović E, Schremb M, Tuković Ž, Jakirlić S, Tropea C. 2018 Computational modeling of freezing of supercooled water using phase-field front propagation with immersed points. *International Journal of Multiphase Flow* **99**, 329–346.
22 de Rosa D, Capizzano F, Cinquegrana D. 2023 Multi-step Ice Accretion by Immersed Boundaries. Technical report SAE Technical Paper.
23 Paz PE, Radenac E, Péron S, Blanchard G, Laurendeau E, Villedieu P. 2023 3D Immersed Boundary Methods for the Calculations of Droplet Trajectories towards Icing Application. Technical report SAE Technical Paper.
24 Patankar SV, Spalding D. 1972 A calculation procedure for heat, mass and momentum transfer in three-dimensional parabolic flows. *International journal of heat and mass transfer* **15**, 1787–1806. (10.1016/0017-9310(72)90054-3)
25 Issa RI. 1986 Solution of the implicitly discretised fluid flow equations by operator-splitting. *Journal of computational physics* **62**, 40–65. (10.1016/0021-9991(86)90099-9)
26 Jasak H. 1996 *Error analysis and estimation for the finite volume method with applications to fluid flows*. Ph.d. thesis Imperial College London.
27 Wright WB. 1995 Update to the NASA Lewis Ice Accretion Code LEWICE. Contractor Report NASA-CR-198355 NYMA, Inc.
28 Jones KF. 1990 The density of natural ice accretions related to nondimensional icing parameters. *Quarterly Journal of the Royal Meteorological Society* **116**, 477–496. (10.1002/qj.49711649212)
29 Macklin WC. 1962 The density and structure of ice formed by accretion. *Quarterly Journal of the Royal Meteorological Society* **88**, 30–50. (10.1002/qj.49708837504)
30 Weller H, Tabor G, Jasak H, Fureby C. 1998 A tensorial approach to computational continuum mechanics using object orientated techniques. *Computers in Physics* **12**, 620–631.
31 Jasak H, Jemcov A, Tukovic Z. 2007 OpenFOAM: A C++ Library for Complex Physics Simulations. In *Coupled Methods in Numerical Dynamics* Dubrovnik.
32 Jasak H. 2009 OpenFOAM: Open source CFD in research and industry. In *International Journal of Naval Architecture and Ocean Engineering* vol. 1 pp. 89–94.
33 Stefanini LM, Silvares OM, Silva GAL, Zerbini EJGJ. 2007 Convective heat transfer effects in airfoil icing. In *Proceedings of the 19th International Congress of Mechanical Engineering (COBEM 2007)* number COBEM2007-2222 pp. 1–10.
34 Stefanini LM. 2009 Efeitos da camada limite térmica na formação de gelo em aerofólios de uso aeronáutico. Master's thesis Escola Politécnica da Universidade de São Paulo, São Paulo, Brazil.
35 Tukovic Z, Jasak H. 2008 Simulation Of Free-rising Bubble With Soluble Surfactant Using Moving Mesh Finite Volume/area Method. In *6th International Conference on CFD in Oil & Gas, Metallurgical and Process Industries* Trondheim.
36 Silva GAL, Silvares OM, Zerbini EJGJ, Hefazi H, Chen HH, Kaups K. 2009 Differential Boundary-Layer Analysis and Runback Water Flow Model Applied to Flow Around Airfoils with Thermal Anti-ice. In *AIAA Aerospace Sciences and Meeting* number 2009-3967 pp. 1–12. (10.2514/6.2009-3967)
37 Jasak H, Rigler D, Tuković 2014 Design and implementation of Immersed Boundary Method with discrete forcing approach for boundary conditions. In *11th World Congress on Computational Mechanics - WCCM XI* Barcelona.
38 Wright WB. 2005 Validation Results for LEWICE 3.0. NASA Contractor Report NASA/CR-2005-213561 NASA Cleveland, OH, United States. Available at NASA Technical Reports Server (NTRS).
39 Papadakis M, Breer M, Craig N, Liu X. 1994 Experimental Water Droplet Impingement Data on Airfoils, Simulated Ice Shapes, an Engine Inlet and a Finite Wing. Contractor Report NASA-CR-4636 NASA. DOT/FAA/CT-TN93/18, E-9254.

40 Langmuir I, Blodgett K. In Suits CG, Way HE, editors, *Atmospheric Phenomena* , pp. 335–347. Elsevier. Mathematical Investigation of Water Droplet Trajectories (10.1016/b978-0-08-009362-8.50021-1)

41 Shin J, Bond TH. 1992 Experimental and Computational Ice Shapes and Resulting Drag Increase for a NACA 0012 Airfoil. Technical Memorandum TM-105743 National Aeronautics and Space Administration (NASA) Cleveland. NASA TM-105743. Presented at the 5th Symposium on Numerical and Physical Aspects of Aerodynamic Flows sponsored by California State University Long Beach, California, January 13-16, 1992.

42 Emmons HW. 1948 Flow of a Compressible Fluid past a Symmetrical Airfoil in a Wind Tunnel and in Free Air. Technical Note NACA TN 1746 National Advisory Committee for Aeronautics Washington, DC.

43 Al-Khalil KM, Horvath C, Miller DR, Wright WB. 2001 Validation of NASA Thermal Ice Protection Computer Codes. Part 3: The Validation of Antice. Technical Memorandum NASA TM-2001-210907 National Aeronautics and Space Administration (NASA) Cleveland.

44 Shih TH, Liou WW, Shabbir A, Yang Z, Zhu J. 1995 A New $k-\epsilon$ Eddy Viscosity Model for High Reynolds Number Turbulent Flows. *Computers & Fluids* **24**, 227–238.

45 Shin J, Bond TH. 1992 Results of an Icing Test on a NACA 0012 Airfoil in the NASA Lewis Icing. In *30th Aerospace Sciences Meeting and Exhibit* number AIAA-92-0647. American Institute of Aeronautics and Astronautics.

46 Hestenes MR, Stiefel E. 1952 Methods of Conjugate Gradients for Solving Linear Systems. *Journal of Research of the National Bureau of Standards* **49**, 409–436.

47 Ruge J, Stüben K. 1987 Algebraic Multigrid (AMG). *Multigrid Methods* **3**, 73–130.

48 Stüben K. 1999 A Review of Algebraic Multigrid. *Journal of Computational and Applied Mathematics* **128**, 281–309.

49 Spalding DB. 1972 A Novel Finite Difference Formulation for Differential Expressions Involving Both First and Second Derivatives. *International Journal for Numerical Methods in Engineering* **4**, 551–559.

50 Van Leer B. 1979 Towards the Ultimate Conservative Difference Scheme V. A Second Order Sequel to Godunov's Method. *Journal of Computational Physics* **32**, 101–136.

51 Van Leer B. 1982 Flux-Vector Splitting for the Euler Equations. *Lecture Notes in Physics* **170**, 507–512.

52 Roe PL. 1986 Characteristic-Based Schemes for the Euler Equations. *Annual Review of Fluid Mechanics* **18**, 337–365.

53 Leonard BP. 1991 The ULTIMATE Conservative Difference Scheme Applied to Unsteady One-Dimensional Advection. *Computer Methods in Applied Mechanics and Engineering* **88**, 17–74.

54 Menter FR. 1994 Two-equation eddy-viscosity turbulence models for engineering applications. *AIAA Journal* **32**, 1598–1605. (10.2514/3.12149)

55 Spalart PR, Allmaras SR. 1992 A One-Equation Turbulence Model for Aerodynamic Flows. *La Recherche Aerospatiale* pp. 5–21.

56 Federal Aviation Administration. 2007 Aircraft Ice Protection. Advisory Circular 20-73A. [Online]. Available: https://www.faa.gov/documentLibrary/media/Advisory_Circular/AC_20-73A.pdf.

57 Drela M. 1989 XFOIL: An Analysis and Design System for Low Reynolds Number Airfoils. In Mueller TJ, editor, *Low Reynolds Number Aerodynamics*, Lecture Notes in Engineering, vol. 54, . Berlin, Heidelberg: Springer. (10.1007/978-3-642-84010-4_1)

58 Karman Tv, Tsien Hs. 1938 The fundamental principles of flow in the boundary layer in compressible fluids. *Journal of the Aeronautical Sciences* **5**, 227–240.

59 Glauert H. 1928 Approximate calculation of the lift of an airfoil in a compressible flow. Technical report NACA TM-562. Translated from "Die Gesetze des Luftwiderstandes," ZFM, Vol. 4, No. 1, 1923.